ARTICLE IN PRESS

ELSEVIER

Journal of Biomechanics ∎ (∎∎∎∎) ∎∎∎–∎∎∎

JOURNAL OF BIOMECHANICS

www.elsevier.com/locate/jbiomech
www.JBiomech.com

Computational modeling of multicellular constructs with the material point method

James E. Guilkey[a], James B. Hoying[b], Jeffrey A. Weiss[c,*]

[a]Department of Mechanical Engineering, The University of Utah, 50 South Central Campus Drive, Room 2202, Salt Lake City, Utah 84112, USA
[b]Regenerative Medicine Program, BIO5 Institute, University of Arizona, Arizona Health Sciences Center , Room 5302, 1501 N. Campbell, P.O. Box 245084, Tucson, Arizona 85724, USA
[c]Department of Bioengineering, and Scientific Computing and Imaging Institute, The University of Utah, 50 S Central Campus Dr Room 2480, Salt Lake City, UT 84112, USA

Accepted 10 June 2005

Abstract

Computational modeling of the mechanics of cells and multicellular constructs with standard numerical discretization techniques such as the finite element (FE) method is complicated by the complex geometry, material properties and boundary conditions that are associated with such systems. The objectives of this research were to apply the material point method (MPM), a meshless method, to the modeling of vascularized constructs by adapting the algorithm to accurately handle quasi-static, large deformation mechanics, and to apply the modified MPM algorithm to large-scale simulations using a discretization that was obtained directly from volumetric confocal image data. The standard implicit time integration algorithm for MPM was modified to allow the background computational grid to remain fixed with respect to the spatial distribution of material points during the analysis. This algorithm was used to simulate the 3D mechanics of a vascularized scaffold under tension, consisting of growing microvascular fragments embedded in a collagen gel, by discretizing the construct with over 13.6 million material points. Baseline 3D simulations demonstrated that the modified MPM algorithm was both more accurate and more robust than the standard MPM algorithm. Scaling studies demonstrated the ability of the parallel code to scale to 200 processors. Optimal discretization was established for the simulations of the mechanics of vascularized scaffolds by examining stress distributions and reaction forces. Sensitivity studies demonstrated that the reaction force during simulated extension was highly sensitive to the modulus of the microvessels, despite the fact that they comprised only 10.4% of the volume of the total sample. In contrast, the reaction force was relatively insensitive to the effective Poisson's ratio of the entire sample. These results suggest that the MPM simulations could form the basis for estimating the modulus of the embedded microvessels through a parameter estimation scheme. Because of the generality and robustness of the modified MPM algorithm, the relative ease of generating spatial discretizations from volumetric image data, and the ability of the parallel computational implementation to scale to large processor counts, it is anticipated that this modeling approach may be extended to many other applications, including the analysis of other multicellular constructs and investigations of cell mechanics.

Keywords: Computational mechanics; Cell mechanics; Confocal microscopy; Meshless methods; Angiogenesis; Capillary

1. Introduction

Cells exhibit a wide range of responses to mechanical conditioning, including modification of the extracellular matrix (ECM) and alterations in cell adhesion and cytoskeletal tension. Thus, the effects of globally applied mechanical loads on local cell stresses and strains are a

*Corresponding author. Tel.: +1 801 587 7833; fax: +1 801 585 5361.
E-mail address: jeff.weiss@utah.edu (J.A. Weiss).

0021-9290/$ - see front matter
doi:10.1016/j.jbiomech.2005.06.017

topic of considerable interest in mechanobiology (Brown, 2000). Globally applied mechanical loading can result in highly inhomogeneous stress and strain fields around cells (Guilak et al., 1999; Wu and Herzog, 2000). Explicit microscale geometric and material representations are needed to calculate the local state of stress that results from globally applied strains and/or forces.

Nearly all studies of the mechanics of cells have used the finite element (FE) method to discretize the governing equations of motion. Although some of the earliest reports of computational modeling of the mechanics of cells date back as far as 15 years (Cheng, 1987), most of the literature is relatively recent. Applications have included the study of leukocyte deformation (Dong and Skalak, 1992), cell–tissue interactions (Barocas and Tranquillo, 1997), intracellular/extracellular fluid flow (Lei et al., 1999), chondrocyte interaction with the pericellular matrix (Wu and Herzog, 2000) and micropipette aspiration (Drury and Dembo, 2001; Shao, 2002). Material parameter estimation with the FE method has been applied at the cellular and subcellular levels to determine material properties of the cell nucleus (Caille et al., 2002) and cochlear outer hair cells (Spector et al., 2002).

The main difficulty with application of the FE method to simulations of the mechanics of cells and cellular constructs is the representation of the highly complex geometry by an unstructured mesh (Breuls et al., 2002). Although geometric information can be obtained from one of a variety of imaging techniques, the process of converting this image data to a suitable unstructured mesh is a time consuming process that requires sophisticated software to first extract iso-surfaces and then generate a robust mesh within each region. Automation of the FE mesh generation process is notoriously difficult and a significant portion of analysis time is spent simply on mesh generation.

Additional complications arise when considering the use of FE methods to study cellular constructs. Examples of cellular constructs include three-dimensional cell cultures (Baer et al., 2001; Cacou et al., 2000; Fournier and Doillon, 1992; Korff and Augustin, 1999; Prajapati et al., 2000; Wakatsuki et al., 2000) and tissue cultures (Seliktar et al., 2000; Shepherd et al., 2004; Zhu et al., 2000). For example, mesh generation for the simulation of the mechanics of cells embedded in a real or surrogate ECM material is especially difficult, since ideally FE meshes should be compatible at material interfaces. The representation of interface conditions such as sliding contact between materials is difficult, since explicit boundaries of the materials or structures must be defined for FE contact algorithms. Also, the FE method can suffer from issues of mesh entanglement (i.e., element inversion) when local stresses/strains are extremely large. This type of localization is to be expected at the interface between highly deformable materials with different material properties. These difficulties make the use of the FE method for modeling cellular constructs difficult at best, and often completely infeasible.

Meshless methods (e.g., (Belytschko et al., 1996; Li and Liu, 2002)) can circumvent all of these complications. In particular, since these methods generally represent material geometry by a collection of particles, they require much less sophisticated tools to generate a geometric representation, and meshless methods are not subject to deficiencies such as mesh entanglement and hour glassing (Doblare et al., 2005). Lastly, since knowledge of material type is carried on particles, explicit knowledge of interface locations is not required to model contact (Bardenhagen et al., 2001). While no computational method is without its shortcomings, meshless methods constitute a relatively new set of tools that may circumvent problems encountered in traditional FE analysis of cell mechanics and multicellular constructs. Although strategies such as adaptive mesh refinement (AMR) have been developed within the FE framework to alleviate some of these problems, these strategies are relatively complicated, difficult to implement for parallel-distributed computation and often introduce error into the solution.

The computational method employed in the current study is the Material Point Method (MPM). MPM, as first described by Sulsky (Sulsky et al., 1994; Sulsky et al., 1995), is a particle-based method for simulations in computational solid and fluid mechanics using explicit time integration. In MPM, the principal variables all exist on particles, (which are not explicitly connected), while a background grid is used as a computational "scratchpad". The desire to study static and low-rate dynamic loading conditions with MPM motivated the development and implementation of an implicit time integration strategy (Guilkey and Weiss, 2003). The objectives of this research were: (1) to present the implicit MPM and to describe a modification to the algorithm that improves its accuracy and robustness for analysis of multicellular constructs, (2) to describe a method to analyze specimen-specific mechanics of multicellular constructs with MPM, using volumetric image data as a source of geometry, (3) to demonstrate the feasibility of this approach by applying it to study the mechanics of vascularized constructs using parallel distributed computing, and (4) to conduct convergence and material sensitivity studies.

2. Materials and methods

2.1. Implicit MPM

MPM is a variant of particle-in-cell (PIC) methods (Harlow, 1964) that represent materials as a collection of particles (material points) instead of connected elements. MPM differs from traditional PIC in that, rather than simply tracking the particle position and mass, MPM particles carry the full physical state of the material, including mass, volume, velocity, temperature, stress, etc. A regular structured grid is used as a computational scratchpad for integration and solution of the weak form of the equations of motion. The description below assumes quasi-static conditions and elastic material behavior to simplify the presentation and clarify its use in the context of the present analyses, although it should be noted that our implementation accommodates inertial effects and any constitutive model can be easily implemented. For a complete depiction of the algorithm including inertial effects and for arbitrary constitutive models, see (Guilkey and Weiss, 2003).

Although implicit time integration can be used for any rate of loading, it is more efficient for analyses when the relative rate of loading is slow with respect to the wavespeed of the material. This class of problems includes quasi-static and low-rate dynamic loading. For faster rates of loading, explicit time integration is computationally more efficient (Sulsky et al., 1994). In implicit time integration, a "time step" represents either an increment in loading for quasi-static analysis or an increment in loading and/or time for a dynamic analysis. For each time step, the increment in displacement on the grid that minimizes the energy of the system is determined via a nonlinear iterative solution procedure based on Newton's method or a quasi-Newton method, and this increment in displacement is subsequently used to update the particle positions. Assuming that a converged solution is available at time t, the algorithm to obtain a solution at time t+dt can be described by the following steps (Fig. 1):

(1) Initialization phase: The incremental displacement vector $\Delta \boldsymbol{u}_g^0(t+dt)$ is initially zero, unless displacements are prescribed for part of the domain. The particle external forces $\boldsymbol{Fext}_p(t+dt)$ are interpolated to the computational grid to yield the external forces on the grid, $\boldsymbol{Fext}_g(t+dt)$ (Fig. 1, panel 2). A grid node receives contributions from particles that are currently residing in grid cells that are constructed with that node, projected via the standard linear FE style shape functions S_{gp}:

$$\boldsymbol{Fext}_g(t+dt) = \sum_p S_{gp} \boldsymbol{Fext}_p(t+dt). \tag{1}$$

The subsequent steps take place iteratively until the optimal incremental displacement vector $\Delta \boldsymbol{u}_g^k(t+dt)$ is found, where the superscript k refers to the iteration number.

(2) Compute the deformation gradient $\boldsymbol{F}_p^k(t+dt)$ at current particle locations $\boldsymbol{x}_p(t)$ using $\boldsymbol{\Delta u}_g^k(t+dt)$ and the deformation gradient from the previous timestep:

$$\boldsymbol{F}_p^k(t+dt) = \boldsymbol{dF}_p^k(dt)\boldsymbol{F}_p(t) = (\boldsymbol{G}_{gp}\boldsymbol{\Delta u}_g^k(t+dt) + \boldsymbol{1})\boldsymbol{F}_p(t). \tag{2}$$

Here, $\mathbf{G}_{gp}$ is a matrix containing gradients of the shape functions S_{gp} evaluated at current particle locations and $\boldsymbol{1}$ is the 2nd-order identity tensor. The Cauchy stress $\boldsymbol{\sigma}_p^k(\boldsymbol{F}_p^k(t+dt))$ and spatial elasticity tensor

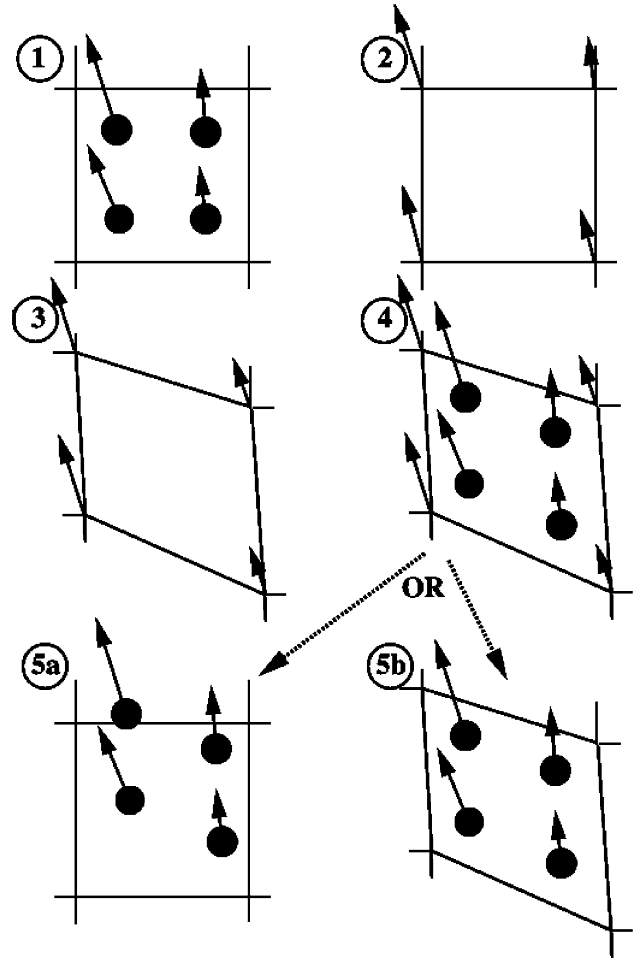

Fig. 1. Illustration of the steps in the MPM algorithm for particles occupying a single cell of the background grid. (1) A representation of four material points (filled circles), overlayed with the computational grid (solid lines). Arrows represent displacement vectors. (2) The material point state vector (mass, volume, velocity etc.) is projected to the nodes of the computational grid. (3) The discrete form of the equations of motion is solved on the computational grid, resulting in updated nodal velocities and positions. (4) The updated nodal kinematics are interpolated back to the material points, and their state is updated. (5a). In the standard MPM algorithm, the computational grid is reset to its original configuration, and the process is repeated, (5b) In the modification algorithm described herein, the grid is not reset, but is allowed to move with the particles, thereby retaining the optimal distribution of particles with respect to the grid.

$\boldsymbol{D}_p^k(\boldsymbol{F}_p^k(t+dt))$ are then calculated from the constitutive model.

(3) The internal force vector $\boldsymbol{Fint}_p^k(t+dt)$ and tangent stiffness matrix $\boldsymbol{KK}_g^k(t+dt)$ are evaluated on the grid:

$$\boldsymbol{Fint}_g^k(t+dt) = \sum_e \int_{\Omega e} \boldsymbol{B}_L^T \boldsymbol{\sigma}_p^k \, \mathrm{d}v, \tag{3}$$

$$\boldsymbol{KK}_g^k(t+dt) = \boldsymbol{Kmat}_g^k(t+dt) + \boldsymbol{Kgeo}_g^k(t+dt), \tag{4}$$

where

$$\boldsymbol{Kmat}_g^k(t+dt) = \sum_e \int_{\Omega e} \boldsymbol{B}_\mathrm{L}^T \boldsymbol{D}_p^k \boldsymbol{B}_\mathrm{L} \, \mathrm{d}v, \tag{5}$$

$$\boldsymbol{Kgeo}_g^k(t+dt) = \sum_e \int_{\Omega e} \boldsymbol{B}_\mathrm{NL}^T \boldsymbol{\sigma}_p^k \boldsymbol{B}_\mathrm{NL} \, \mathrm{d}v. \tag{6}$$

$\boldsymbol{B}_L$ and $\boldsymbol{B}_{NL}$ are the standard linear and nonlinear strain-displacement matrices encountered in a nonlinear FE formulation (Bathe, 1996) and Σ_e represents assembly of grid cells, processing contributions from grid nodes into the global arrays. The integrals in Eqs. (3)–(6) are computed as a discrete sum over particles.

(4) Solve the discrete equilibrium equations, linearized about the configuration at time t, iteratively for the incremental displacements $\mathrm{d}\boldsymbol{u}_g^k$ using Newton's method:

$$\boldsymbol{KK}_g^k(t+dt)\mathrm{d}\boldsymbol{u}_g^k = \boldsymbol{Fext}_g(t+dt) - \boldsymbol{Fint}_g^k(t+dt). \tag{7}$$

In the present research, the solution of the linear system in Eq. (7) for the vector $\mathrm{d}\boldsymbol{u}_g^k$ was performed using a conjugate gradient solver with a Jacobi preconditioner (Balay et al., 2002). The nodal displacements are accumulated each iteration by

$$\Delta\boldsymbol{u}_g^{k+1}(t+dt) = \Delta\boldsymbol{u}_g^k(t+dt) + \boldsymbol{du}_g^k, \tag{8}$$

Steps 2–4 are repeated iteratively until $\boldsymbol{du}_g^k$ satisfies the convergence criteria:

$$\frac{\left\|\boldsymbol{du}_g^k\right\|}{\left\|\boldsymbol{du}_g^{\max}\right\|} < \varepsilon_d \quad \text{and} \quad \frac{\left\|\boldsymbol{du}_g^k \mathbf{Q}_g^k\right\|}{\left\|\boldsymbol{du}_g^0 \mathbf{Q}_g^0\right\|} < \varepsilon_e, \tag{9}$$

where $\mathbf{Q}_g^k$ is the right hand side of Eq. (7) and ε_d and ε_e are user-defined tolerances on the displacement and energy norms, respectively.

(5) Upon convergence, $\boldsymbol{F}_p^{k+1}(t+dt)$, $\boldsymbol{Fint}_g^{k+1}(t+dt)$ and $\boldsymbol{KK}_g^{k+1}(t+dt)$ are saved and the particle kinematics are updated (Fig. 1, panel 4):

$$\boldsymbol{u}_p(t+dt) = \boldsymbol{u}_p(t) + \sum_g S_{gp}\Delta\boldsymbol{u}_g, \tag{10}$$

$$\boldsymbol{x}_p(t+dt) = \boldsymbol{x}_p(t) + \sum_g S_{gp}\Delta\boldsymbol{u}_g. \tag{11}$$

(6) The grid is reset to its original (typically rectilinear) configuration (Fig. 1, panel 5a).

(7) Continue to the next time step:

This algorithm was implemented in the Uintah Computational Framework (UCF) (Parker, 2002), an infrastructure for large scale parallel scientific computing on structured Cartesian grids. The UCF uses domain decomposition and the Message Passing Interface (MPI) (Gropp et al., 1996) to achieve parallelism on distributed memory clusters. Because the interactions of the particles with the computational grid are local, and due to the simple rectilinear structure of the background grid, parallelism of MPM is simplified. Specifically, the computational grid is easily decomposed spatially into subdomains of grid cells, with each processor performing calculations for a subdomain. In contrast, the solution of the system of linear equations in Eq. (7) is a global operation. For this research, the PETSc suite of linear solvers (Balay et al., 2001) was used to perform the distributed parallel solution of these equations.

2.2. Modified MPM algorithm

The algorithm described above can result in an artifact when particles cross the boundaries of grid cells (Zhou, 1998), which can be especially troublesome for quasi-static simulations since there are no inertial forces. In this research, a modified algorithm was developed and implemented in which the background grid geometry is not reset after each MPM computational cycle (Fig. 1, panel 5b). The goal of this change was to maintain the initial spatial distribution of particles relative to cells in the computational grid. Typically, a computational grid is chosen so that each cell contains the same number of particles. The locations of the particles with respect to the grid nodes do not change when the grid is not reset. In this case, it is not necessary to track the deformation of both the particles and the grid. Rather, by carrying and correctly updating the deformation gradient and the displacement of the particles, the deformed grid can be regenerated at any time. At any point during the simulation, the analyst may choose to reset the grid, either to its original configuration, or to another configuration determined to be optimal. Note that by choosing not to reset the grid, the analyst is making a tradeoff and may encounter problems related to a severely distorted mesh, similar to the types of problems that MPM was created to avoid. The benefits of this modification are demonstrated in the Section 3.

2.3. Example application—in vitro angiogenesis system

The motivation for this research was provided by studies of the interaction of angiogenic microvessels with the ECM and the effects of mechanical conditioning on capillary sprouting using an in vitro model of angiogenesis (Hoying et al., 1996). Vascular endothelial cells are highly sensitive to mechanical loading, which may be generated via flow through blood vessels or through mechanical deformation of the ECM. To examine the mechanical stimuli that promote and inhibit capillary sprouting and to study the biochemical events associated with mechanotransduction, the relationship between globally applied mechanical strain and the mechanical environment at the capillary sprout must be quantified. Further, angiogenic microvessels modify the material properties of the ECM by expression of matrix proteases, and thus changes to the global mechanical response of vascularized constructs reflect the local activity of endothelial cells on the ECM.

The in vitro angiogenesis system involves the culture of intact microvessel elements (specifically, small arterioles and capillaries) isolated from rat adipose, in a three-dimensional collagen gel. Isolated vessel elements contain associated perivascular cells and spontaneously grow as patent tubes through the elaboration of numerous vessel "sprouts". These vessels continue to grow into a new vascular network that ultimately fills the gel space (Fig. 2). Angiogenesis begins, predictably, at day 4 of culture and a uniform vascular network forms by day 14. Based on morphological and immunostaining data, the isolated vessel fragments include the full spectrum of vessel elements in the microvasculature, namely arterioles, capillaries and venules (Hoying et al., 1996). The new and parent vessels retain the ability to form a functional vascular tree following implantation of the vascularized construct (Shepherd et al., 2004), supporting the notion that the microvessels are healthy, normal and functional.

2.4. Confocal imaging and particle generation

A vascularized construct was harvested after 10 days of culture and stained en bloc with endothelial cell-specific lectin GS-1, directly bound to fluorescein. A volumetric confocal image dataset ($512(x) \times 512(y) \times 52(z)$, x–y dimensions $537.6 \times 537.6\,\mu m$, section thickness $1.0\,\mu m$) was obtained with a Bio-Rad MRC-1024ES confocal laser scanning microscope using a 40X objective (Fig. 3, left panel). The z plane thickness of CLSM images was calibrated using 6 and $15\,\mu m$ FocalCheck microspheres (Molecular Probes Inc.).

A 3D hysteresis-thresholding algorithm was used to segment the microvessels in the confocal image dataset. Each voxel was represented by one material point, and material type (either microvessel or collagen) was assigned to each material point based on its fluorescent intensity relative to the threshold value. This resulted in 13.6 million material points to represent the 3D volume of the confocal image (Fig. 3, middle panel). The background grid was constructed so that each grid cell contained $(4 \times 4 \times 2)$ material points, resulting in 426,984 grid cells, 449,307 nodes for the background grid and 1.3 million unknowns (degrees of freedom, DOFs) in the linear system defined by Eq. (7). Microvessel volume fraction was 10.4% for this sample.

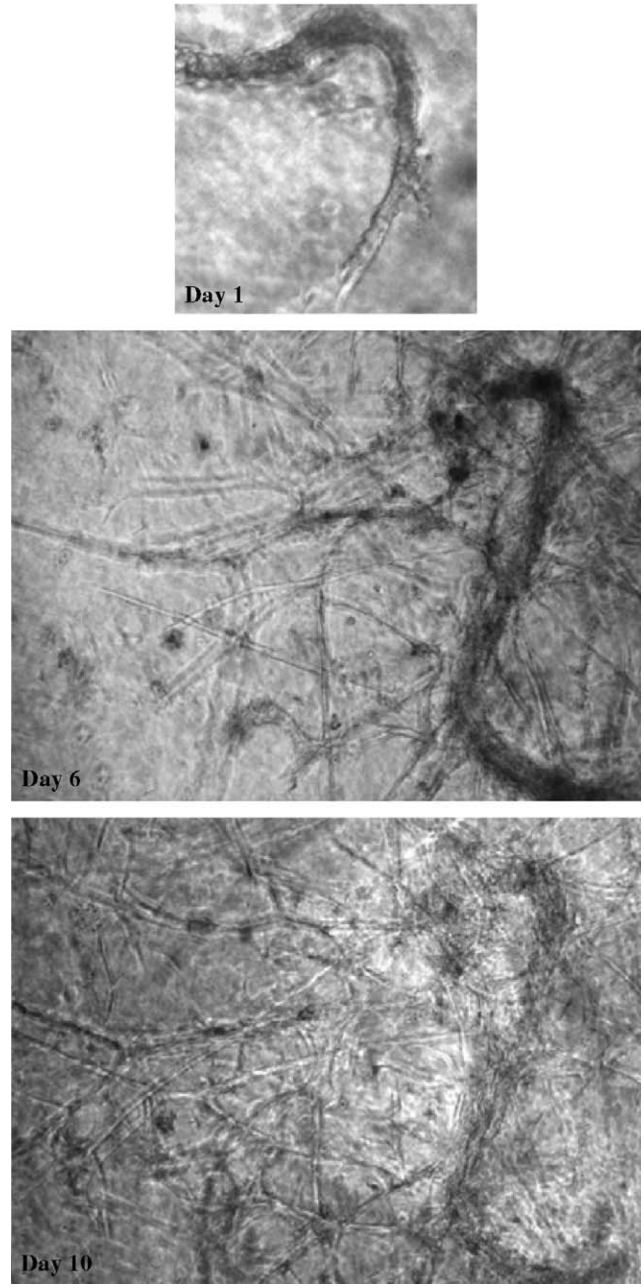

Fig. 2. Phase micrographs of microvessel fragments cultured in 3D collagen gels. Top—typical microvessel fragment at day 1 of culture. Middle, Bottom—formation and branching of microvascular network at days 6 and 10 of culture. Note that the microvessel shown in the top panel is not the same field as shown in the middle and bottom panels.

2.5. Constitutive model and baseline material properties

The material properties of collagen gels are nonlinear and viscoelastic (Krishnan et al., 2004), while there are no data available for the material properties of

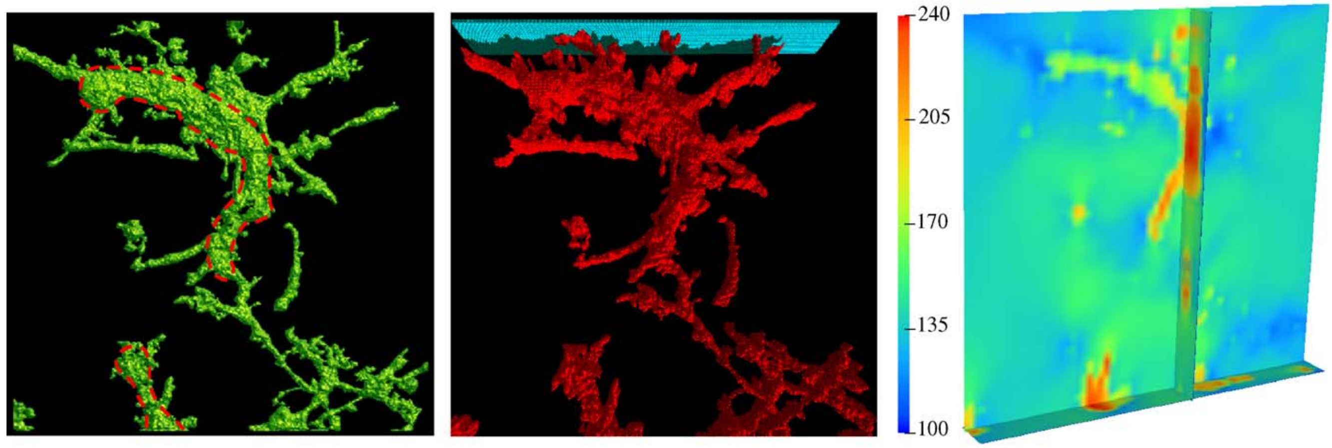

Fig. 3. Left—volume rendering of segmented confocal microscopy data, showing a typical microvascular construct in collagen at day 10 of culture. Dashed red lines indicate approximate boundaries of parent vessels. Middle—initial distribution of material points (collagen material points not shown for clarity), consisting of 13 million particles. Direction of tensile loading is vertical. Right—Distribution of von Mises stress (Pa) for the baseline 3D model under 10% axial extension. Note the highly inhomogeneous stress distribution and the vertical channeling of stresses through the microvessels.

individual microvessel fragments. As a first order approximation, an uncoupled compressible neo-Hookean hyperelastic constitutive model was used to represent both the collagen and the microvessels, with strain energy W (Simo and Hughes, 1998)

$$W = U(J) + \tilde{W}(\tilde{\mathbf{C}}). \tag{12}$$

Here $\tilde{W}(\tilde{\mathbf{C}}) = (\mu/2)(I_1 - 3), U(J) = (k/2)[\ln(J)]^2$, J is the volume ratio, μ is the shear modulus, k is the bulk modulus and $\tilde{I}_1 = \mathrm{tr}(\tilde{\mathbf{C}})$ is the 1st invariant of the deviatoric right deformation tensor $\tilde{\mathbf{C}}$. The shear modulus of the collagen gel ($\mu_c = 520.8$ Pa) was based on our experimental data (Krishnan et al., 2004). For the baseline 3D analysis described below, the shear modulus of the microvessels μ_v was assumed to be twice the value of the collagen gel. The bulk modulus for both the collagen and the microvessels was unknown and was initially chosen to be twice the shear modulus, yielding an effective Poisson's ratio of $\nu = 0.29$. Additional analyses were performed with all particles assigned the material properties of collagen for comparison.

2.6. Details of the 3d computational analysis

Ongoing experiments on the vascularized constructs include endpoint viscoelastic tensile testing to assess the effects of microvessel sprouting on ECM material properties (Krishnan et al., 2003a, b) and mechanical conditioning via tensile testing during the culture of the constructs. To simulate axial extension of the vascular construct, the bottom of the computational domain was constrained and a vertical displacement was prescribed to material points along the top of the computational domain to achieve 10% global tensile strain. To assess the ability of the execution time to scale with the number of processors used, the three dimensional nonlinear analysis was performed on 20, 40, 60, 80, 120, 160 and 200 processors of a 1024 processor distributed memory Linux cluster (Opteron 240 CPUs, 1.4 GHz), using MPI to achieve parallelism. Results were processed to determine reaction force at the clamped end and spatial distribution of von Mises stress.

2.7. Effects of grid resolution

Because our research on the effects of mechanical conditioning on vascularized constructs will eventually require large numbers of specimen-specific 3D simulations, the effects of grid resolution and particle distribution on the quality of the simulation results and the time needed to obtain a solution were examined. To assess the quality of the solution, a convergence study was performed to assess the effects of these factors on the resulting reaction force and von Mises stress distribution. These studies were performed in 2D using a particle distribution that was based on one slice from the 3D confocal image dataset.

Each of the 2D simulations was carried out using the same spatial distribution of particles, while the resolution of the background grid was varied (Fig. 4). Since the equations of motion are solved on the background grid, its resolution determines the spatial accuracy of the solution. Further, because the grid resolution determines the size of the linear system, solution time depends most strongly on grid resolution rather than the number of particles. The 2D slice was discretized using 64^2, 128^2 and 256^2 grid cells, corresponding to particle distributions of 8×8, 4×4 and 2×2 within

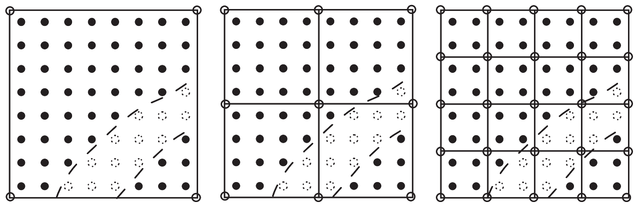

Fig. 4. Schematic of particle and grid configurations investigated in the resolution studies. The spatial volume of the depicted domain is $8.4 \times 8.4 \times 1.0\,\mu m$ in all cases. Dashed lines represent a material boundary. Filled circles and open dashed circles represent material points of two different materials. Open circles with solid lines are nodes in the computational grid. Solid straight lines denote the boundaries of grid cells.

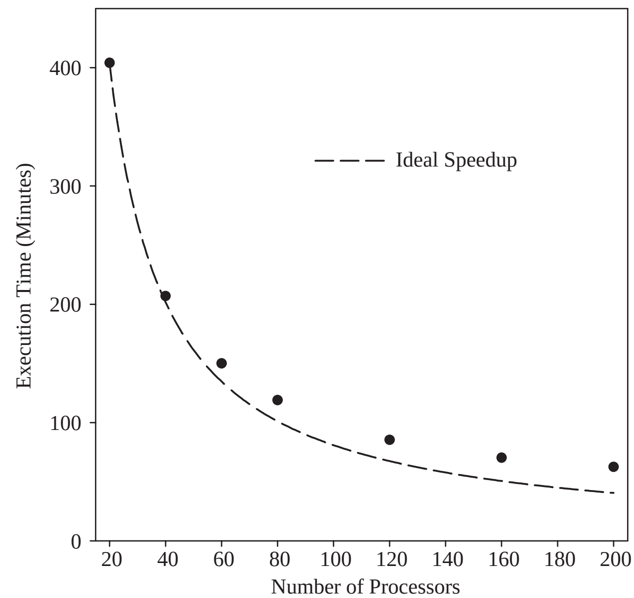

Fig. 5. Effect of number of processors used in simulation on execution time for the 3D simulation. Dashed line represent ideal speedup, which means that doubling the number of processors would result in halving the execution time.

each cell, respectively. The number of particles for all 2D simulations was 250,000. For each discretization, simulations were carried out using a sample that consisted only of collagen, as well as the distribution of collagen and microvessels indicated for the chosen slice of the volumetric dataset. Each case was analyzed using both the traditional MPM algorithm and the modified algorithm described above. The 2D simulations were performed using four processors and the time to solution was recorded.

2.8. Sensitivity to material properties

In addition to the sensitivity to mesh resolution, it is also important to understand how the MPM predictions were affected by the assumed material properties of the microvessel fragments. Simulations were performed for several ratios of relative shear modulus of the collagen μ_c to that of the vessel μ_v ($\mu_v = q\mu_c$ where $q = 0.5$, 1.0, 2.0 and 5.0). For each case, the bulk modulus was adjusted to maintain a Poisson's ratio of 0.29. Another set of simulations was performed in which the relative shear moduli were maintained at $\mu_v = 2\mu_c$, but the bulk moduli were varied to obtain Poisson's ratios of 0.13, 0.29, 0.45 and 0.48. Since the material properties of the microvessels were unknown, these simulations were intended to serve as a guide for designing simulations and experiments in the future, in that they reveal the sensitivity of the simulations to the material properties of the constituents.

3. Results

3.1. Three-dimensional analysis

The baseline 3D computation required 3.4 h of wall clock time on 40 processors. Results indicated a highly inhomogeneous stress distribution in which the microvessels were subjected to a much higher stress than the surrounding collagen (Fig. 3, right panel). This supports the hypothesis that local stresses around cellular constructs in a 3D matrix are inhomogeneous, even for uniaxial tensile loading. The time for the simulation scaled well with the number of processors (Fig. 5). Efficiency for 60, 120 and 200 processors was 90%, 75% and 50%, respectively, in comparison to the 20 processor analysis. The primary reason for the drop-off in efficiency at larger processor counts is the small amount of computation required of each processor in comparison to communication overhead. For comparison, simulations using 20 processors resulted in each processor performing computations for 21,300 grid cells per processor, while simulations using 200 processors resulted in only 2,130 grid cells per processor.

3.2. Effects of computational algorithm

There were substantial visual differences in the spatial distribution of von Mises stress between the simulations that used the standard MPM algorithm versus those that used the modified algorithm. The standard MPM algorithm yielded a stress field that contained substantial artifacts, resulting from particles crossing grid cells when the computational grid was reset (Fig. 6, left panel). The artifacts were of comparable magnitude as the fluctuations in stress that arise due to the inhomogeneous nature of the materials, rendering the results unacceptable. In contrast, with the modified algorithm,

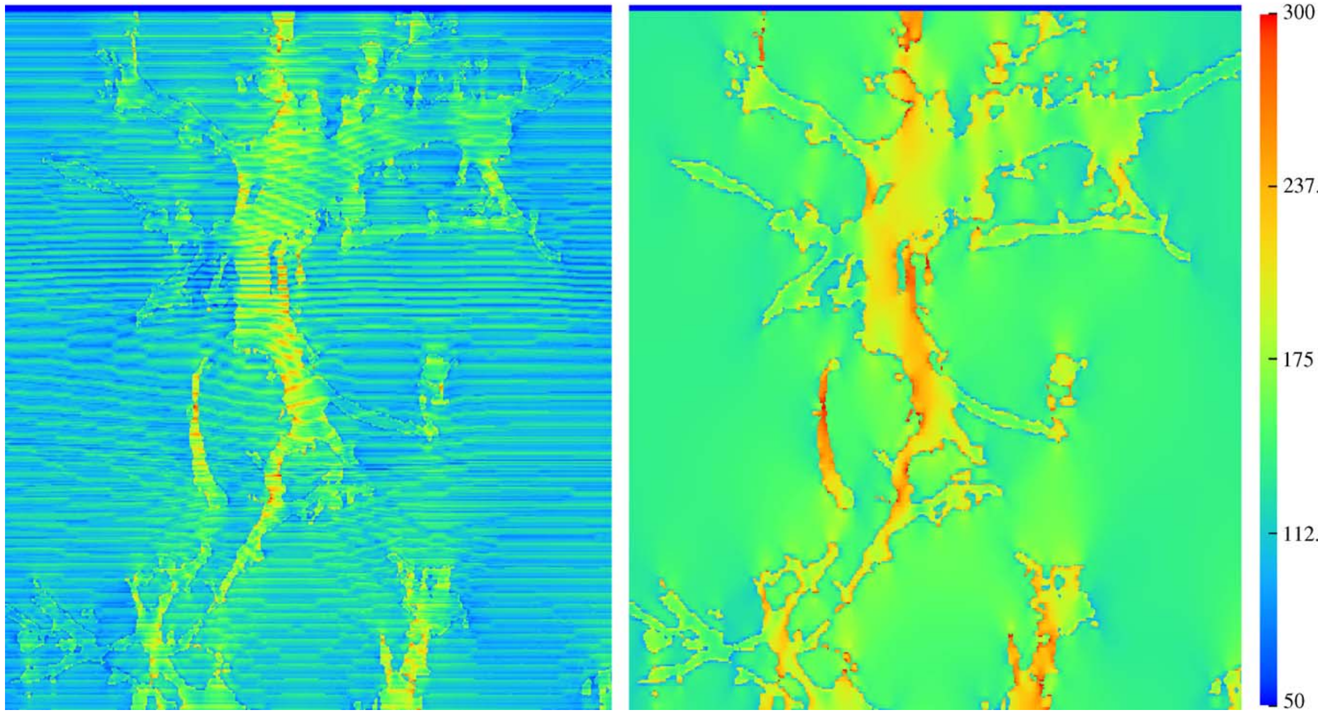

Fig. 6. Effect of resetting the grid during the MPM solution process on the spatial distribution of von Mises stress (Pa). Left panel—standard MPM algorithm resets the grid, resulting in significant artifacts in the stress field due to particles crossing grid boundaries. Right panel—results without resetting the grid. Stress field artifact is eliminated and the resulting stress field is highly inhomogeneous based on the topography of microvessels.

the artifacts were absent and the highly inhomogeneous nature of the stress distribution was apparent (Fig. 6, right panel).

Quantitative evidence of the effectiveness of the algorithmic modification can be found by examination of the reaction force at the constrained end. When the grid was reset after each timestep, the results were extremely unpredictable and showed no signs of convergence with increasing resolution (Fig. 7, left panel). In fact, when the grid was reset for the finer resolution cases, converged solutions at large deformations were, at times, not achieved. Thus the traditional MPM algorithm was neither accurate nor robust. In contrast, when the grid was not reset, convergent behavior was observed and the reaction force increased approximately linearly with the applied strain, consistent with the quasilinear behavior of the neo-Hookean constitutive model (Fig. 7, right panel).

3.3. Effects of grid resolution

Using the modified MPM algorithm, the time to solution for the 2D simulation at 10% strain was 0.3, 0.8 and 5.5 h for the three resolutions in Fig. 4 from coarsest to finest, on 4 processors. Clearly, use of the highest resolution in Fig. 4 came at a significant computational cost, so a closer examination of the results was required to indicate the overall value of high-resolution simulations.

The accuracy of the solutions can be compared by examining the reaction force as a function of applied tensile strain for the different resolutions (Fig. 7, right panel). There was very little difference in the reaction force between the three homogeneous cases or between those cases containing both collagen and microvessel. When the reaction force was compared for the homogeneous and inhomogeneous cases at the same resolutions, the relative difference between the collagen only cases and the collagen with vessel cases was 14.7%, 14.1% and 13.7% from the coarsest resolution to the finest, respectively. The small difference between these values suggests that all three resolutions were converged in terms of prediction of reaction force.

Qualitatively, the differences in spatial distribution of von Mises stress for the three mesh resolutions were subtle (Fig. 8), although there was some evidence of a homogenizing effect on the stress field when cells contained a large number of particles, as in the coarsest case. In all cases, it was evident that the microvessels were subjected to significantly higher stresses. Quantitatively, the three solutions again indicated convergence as the maximum stresses for the three cases were similar (357, 384 and 380 Pa, from coarsest to finest).

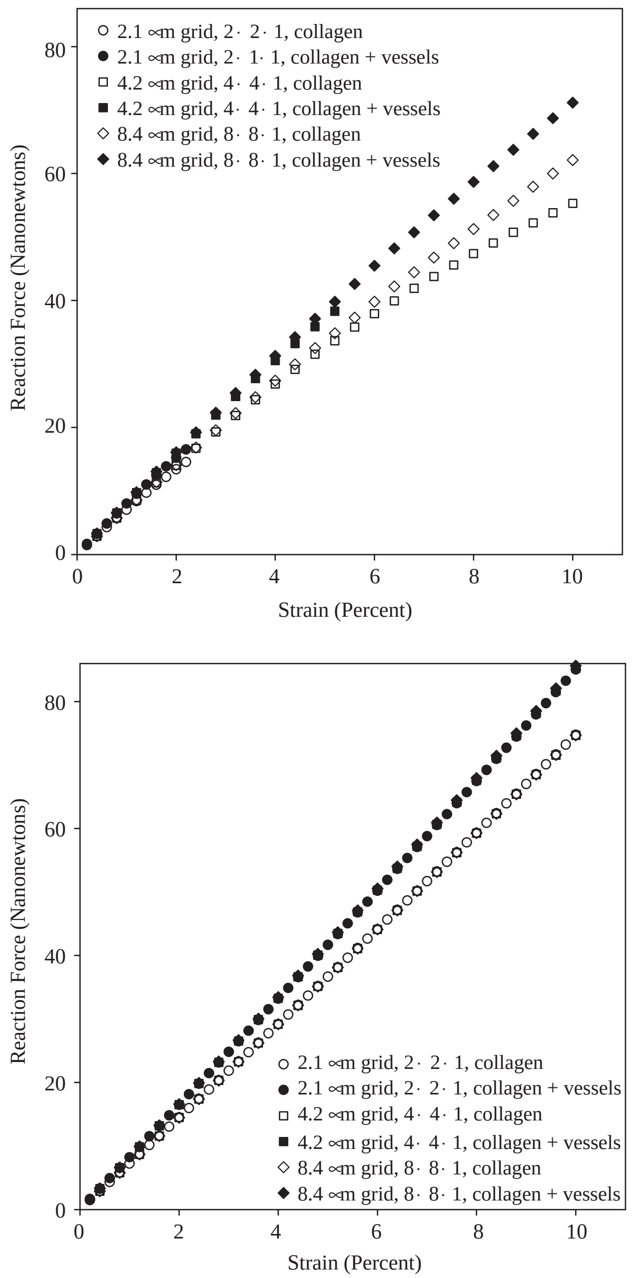

Fig. 7. Effects of solution algorithm, grid resolution and presence of vessels on the reaction force (nN) at the clamped end. All data are for the case of microvessels with a shear modulus that was twice as large as that of the collagen. Top—results for standard MPM algorithm (reset). Bottom—results for modified algorithm (no reset). Left graph shows significant softening of the force-displacement behavior due to particles crossing cell boundaries. This problem was somewhat alleviated when the ratio of particles-per-cell to grid cell size was maximized. Converged solutions could not be obtained for the cases that used the 2.1 μm grid past 2% axial strain, and for the 4.2 μm grid for the "collagen + vessels" case past 5% axial strain. Right—all three resolutions gave acceptable predictions of the force-displacement behavior when the modified MPM algorithm was used. For the analyses that used the modified algorithm, the presence of microvessels increased the peak reaction force by approximately 14%.

3.4. *Sensitivity to material properties*

There was a fairly strong dependence of the reaction force on the stiffness of the microvessels (Table 1), despite the fact that they comprised only 10.4% of the volume of the total sample. The reaction force was less sensitive to Poisson's ratio of the entire sample than to the stiffness of the microvessels (Table 2).

4. Discussion

The approach that was used in this research to convert volumetric image data to a particle representation for use with MPM (or any meshless method) is quite general. Image data may be provided by nearly any type of imaging modality, including CT, MRI or ultrasound. Depending on the image quality, additional image processing may be necessary to distinguish regions of different materials. The quality of the confocal image dataset used in the current study allowed the use of a simple thresholding technique; all materials were classified as either collagen or vessel. However, by using multiple fluorophores, each of which binds to a different protein, it is possible to further refine the material classification to include multiple types of cells or cellular organelles, depending on the physical scale of the simulation. In the context of the confocal image data of the vascularized constructs, we have already succeeded in using two fluorophores to distinguish endothelial cells from smooth muscle cells (Shepherd et al., 2004). Furthermore, additional refinements to the material point distribution may be made based on further processing of the image data. For instance, large gradients in the image intensity indicate material boundaries, and thus the gradient information could be used to provide a denser distribution of material points near these locations to better resolve material interfaces.

Given the relatively small wall clock time that was required for the 3D simulation (3.4 h on 40 processors) in comparison to the resources that are available, both at our site and at national supercomputing centers, simulations that encompass much larger 3D geometries will be possible with implicit MPM. Good scaling was achieved, and at this time, no barriers are evident to inhibit scaling to a larger set of resources. In the context of simulations of the mechanics of vascular constructs, increasing the size of the geometry that is simulated will better reflect the physical tensile experiments that are being performed on the constructs. Also, the ability to address larger geometries increases the range of system types that can be studied with this approach.

When using the traditional MPM algorithm, the cases with higher spatial refinement failed to converge at lower levels of global strain than the less refined cases

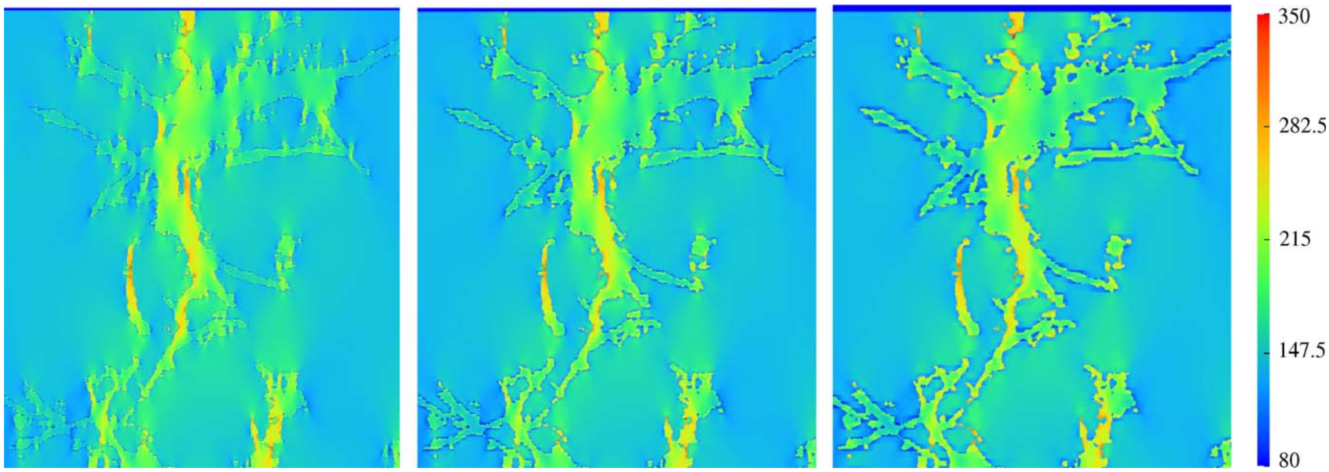

Fig. 8. Effects of grid resolution on von Mises stress distribution. The salient features of the stress field are apparent for even the most coarse resolution case. Namely, stress channeling through the stiff material and the low stress "shadows" that surround these regions are more sharply defined in the higher resolution cases, but the improvement in solution at the highest resolution is marginal and not sufficient to warrant the additional computational cost.

Table 1
Effect of the ratio of the shear modulus of the microvessels (μ_v) to that of the collagen gel (μ_c) on reaction force at 10% tensile strain

μ_v/μ_c	Reaction Force (nN)
0.5	65.0
1.0	74.7
2.0	85.2
5.0	101.4

The bulk moduli of both materials were varied to keep the Poisson's ratio of both materials the same (0.29).

Table 2
Effect of the Poisson's ratio of both the vessels and collagen on the reaction force at 10% strain

Poisson's ratio	Reaction Force (nN)
0.13	73.9
0.29	85.2
0.45	97.7
0.48	99.7

Results indicate a substantially lower degree of sensitivity to this variable than to the shear modulus of the vessels.

(Fig. 7, left panel). This may seem paradoxical at first; however, the failure of those simulations is due to particles crossing from one cell to another. MPM uses linear shape functions on the background grid, the gradients of which are constant (in 1D). These gradients constitute the entries of the strain-displacement matrix in Eq. (3). For the case of a quasi-static loading scenario that should generate a homogeneous stress state for all particles, a uniform distribution of particles will lead to the desired result that the internal force ($\boldsymbol{F}_{\text{int}}$) vanishes on the interior nodes (the sign of the shape function gradient changes when moving from one cell to another, causing the contributions from particles in the adjacent cells to cancel out). When the particle distribution is non-uniform, in order to achieve a zero internal force (necessary to achieve convergence) a non-uniform stress results in the material. An excellent description of this phenomenon is given in (Zhou, 1998). For the cases that used a higher resolution for the background grid, the migration of particles from one grid cell to another occurs more quickly during tensile extension. Furthermore, the associated deleterious impact of particle migration is more severe when there are fewer particles in each grid cell. In the most refined cases, there were four particles in each cell, while in the least resolved cases, there were 64 particles in each cell. The advantages of the modified MPM algorithm are clearly demonstrated by the elimination of artifacts in the stress field (Fig. 6) and the fact that converged solutions were obtained for all grid resolutions (Fig. 7, right panel).

When all results are considered, the medium resolution grid (Fig. 4, middle panel) provided the best compromise between reasonable time to solution and the degree to which the overall solution has converged. Given the significantly higher computational cost of carrying out these simulations at the highest resolution, along with the very modest increase in the quality of the results, use of the highest resolution is unjustified and unnecessary. A small improvement in performance may be obtained for all resolutions by using fewer particles while maintaining the same mesh resolution. However, as the mesh resolution is the major determinant of solution time, any reduction would be modest.

The results in Table 1 indicate a strong dependence of the reaction force on the vessel shear modulus, despite the fact that the vessels comprised only about 10% of the total volume of the sample. This suggests that the MPM simulations could form the basis for estimating the effective shear modulus of the microvessels via a parameter estimation strategy. By first performing tensile tests on specimens of vascularized collagen gels, the load-elongation data could be used, along with the known properties of pure collagen, as inputs to a parameter optimization scheme in which numerical simulations of the experiment are performed with varying parameters, to match, as closely as possible, the experimental results. The parameters to be optimized are the material properties of the microvessels. The finding of the strong sensitivity of the reaction forces to the assumed modulus of the vessels provides encouragement to the prospects for success of such an endeavor.

Although a detailed exposition on the strengths and weakness of meshless and quasi-meshless methods in general is beyond the scope of this work (for a review, see (Belytschko et al., 1996)), it is instructive to consider the algorithmic advantages and disadvantages of MPM in particular in comparison to the FE method for the presently considered application. As demonstrated, MPM provides an extremely straightforward method to discretize complex geometry with multiple material types that is highly amenable to use with volumetric image data. The standard MPM algorithm eliminates element inversion by using a computational grid that is reset after each timestep. In the case of the modified MPM algorithm, the improvements gained from the algorithmic modification come at the cost of losing some of the robustness at high levels of deformation. Specifically, since the background grid is not reset, it is possible to invert elements of the background grid under extreme deformation. For the application described herein, this problem was never encountered and thus the modified algorithm provides a favorable tradeoff. If the deformed state of the background grid becomes such that it impedes the procession of the solution, it is straightforward to switch from the modified to the traditional algorithm (and back) Further, since the initial computational grid is rectilinear and all grid elements initially have 90° corners, it is often possible to achieve larger deformations before element inversion than can be achieved with a conforming FE mesh. In the case of the standard FE method, mesh inversion can be mitigated by using adaptive mesh refinement (AMR, or "h-refinement"—e.g., (de Cougny and Shephard, 1999)). However, AMR introduces additional difficulties since an optimal new mesh is ill-defined and interpolation errors are introduced when projecting to a new mesh. For complex geometries such as those considered herein, the process of generating the new mesh is plagued by the same difficulties as generating the initial mesh, and this process is especially difficult in three dimensions. When compared to generating an entirely new FE mesh for use with AMR, the process of resetting the MPM background grid is trivial.

From the point of view of computational efficiency, MPM requires additional computational steps for interpolations to and from particles that are not required with FE methods, as shown in Eqs. (1), (10) and (11). However, the cost of these additional computations is more than made up for by ease of parallelization of the MPM algorithm. The MPM algorithm is easily programmed for parallel, distributed-memory computers by partitioning particle-based and grid-based calculations through decomposition of the computational domain. In contrast, the initial partitioning of a FE mesh is considerably more complicated and requires careful construction to ensure load balancing between processors. The use of AMR with the FE method requires repartitioning for parallel computations and leads to memory fragmentation (Feng et al., 2005; Wissink et al., 2003).

There are several assumptions and limitations associated with the present work that merit discussion. The discretization and assignment of material properties to the collagen and microvessels assumed uniform microvessel material properties, elastic material behavior for both materials and represented the interface between the microvessels and the collagen as perfectly bonded. Clearly, the effective mechanical behavior of the vascularized constructs will depend on the local interface conditions, which are considerably more complicated and include interactions between the ECM and cell surface integrins. Further, it is likely that the material properties of the microvessel fragments are a function of the specific vessel and its state of proliferation. Additionally, the effects of vascular smooth muscle cells, which are present in the cultures, were not considered. Finally, as smaller length scales are considered, it is important to recognize that the approach described here is based upon the assumption that the materials constitute a continuum. The exploration of phenomena at sub-continuum length scales would require the use of additional discretization approaches. For instance, if one wishes to simulate the effects of cytoskeletal components on cell mechanics, the forces associated with passive and active cytoskeletal elements must be included. Approaches to the integration of these phenomena with MPM could follow one of at least two successful strategies: (1) the representation and prediction of the spatial concentration of the cytoskeletal element(s), thus defining a swelling force that results in a local pressure (Bottino et al., 2002), or (2) explicit representation of cytoskeletal components as discrete elements capable of resisting tension and/or compression and capable of generating axial force (Coughlin and

Stamenovic, 2003; Karcher et al., 2003; Spector et al., 2002; Volokh et al., 2002). In both cases, these forces would enter into the discretized equations of motion used in the MPM formulation through the internal force vector in Eq. (3). Despite these assumptions and limitations, the approach used in these simulations provided a reasonable framework for testing the applicability of MPM for large-scale simulations of cellular constructs.

In summary, this study demonstrated the effectiveness of a modified MPM algorithm for the large-scale simulation of the mechanics of cellular constructs. The presence of microvessels in the collagen construct resulted in stress localization and channeling. Larger simulations (i.e., using as many as 30 million material points) should be very feasible on modern distributed memory clusters. The computational framework that was developed in this research is quite general, and it is anticipated that extension to many other applications will be possible, including the analysis of other multicellular constructs and investigations of cell mechanics.

Acknowledgments

Financial support from NIH #R01 HL077683 (JEG, JBH, JAW), NIH #R01 HL67067 (JBH), DOE #W-7405-ENG-48 (JAW, JEG) and NSF-ITR #CTS0218574 (JEG) is gratefully acknowledged. The Arches Metacluster (Center for High Performance Computing, University of Utah) was funded by NIH Grant #RR17214-01. The authors thank the staff of the Scientific Computing and Imaging Institute and the Center for the Simulation of Accidental Fires and Explosions at the University of Utah for assistance with software development.

References

Baer, A.E., Wang, J.Y., Kraus, V.B., Setton, L.A., 2001. Collagen gene expression and mechanical properties of intervertebral disc cell-alginate cultures. Journal of Orthopaedic Research 19, 2–10.

Balay, S., Buschelman, K., Gropp, W.D., Kaushik, D., Knepley, M.G., et al., 2001. PETSc Web page. http://www.mcs.anl.gov/petsc.

Balay, S., Buschelman, K., Gropp, W.D., Kaushik, D., Knepley, M., et al., 2002. PETSc User's Manual. Rep. ANL-95/11—Revision 2.1.3, Argonne National Laboratory.

Bardenhagen, S.G., Guilkey, J.E., Roessig, K.M., Brackbill, J.U., Witzel, W.M., Foster, J.C., 2001. An improved contact algorithm for the Material Point Method and application to stress propagation in granular material. Computer Modeling in Engineering and Sciences 2, 509–522.

Barocas, V.H., Tranquillo, R.T., 1997. A finite element solution for the anisotropic biphasic theory of tissue- equivalent mechanics: the effect of contact guidance on isometric cell traction measurement. Journal of Biomechanical Engineering 119, 261–268.

Bathe, K.-J., 1996. Finite Element Procedures. Prentice-Hall, Englewood Cliffs.

Belytschko, T., Krongauz, Y., Organ, D., Fleming, M., Krysl, P., 1996. Meshless methods: an overview and recent developments. Computer Methods in Applied Mechanics and Engineering 139, 3–47.

Bottino, D., Mogilner, A., Roberts, T., Stewart, M., Oster, G., 2002. How nematode sperm crawl. Journal of Cell Science 115, 367–384.

Breuls, R.G., Sengers, B.G., Oomens, C.W., Bouten, C.V., Baaijens, F.P., 2002. Predicting local cell deformations in engineered tissue constructs: a multilevel finite element approach. Journal of Biomechanical Engineering 124, 198–207.

Brown, T.D., 2000. Techniques for mechanical stimulation of cells in vitro: a review. Journal of Biomechanics 33, 3–14.

Cacou, C., Palmer, D., Lee, D.A., Bader, D.L., Shelton, J.C., 2000. A system for monitoring the response of uniaxial strain on cell seeded collagen gels. Medical Engineering and Physics 22, 327–333.

Caille, N., Thoumine, O., Tardy, Y., Meister, J.J., 2002. Contribution of the nucleus to the mechanical properties of endothelial cells. Journal of Biomechanics 35, 177–187.

Cheng, L.Y., 1987. Deformation analyses in cell and developmental biology. Part I—formal methodology. Journal of Biomechanical Engineering 109, 10–17.

Coughlin, M.F., Stamenovic, D., 2003. A prestressed cable network model of the adherent cell cytoskeleton. Biophysics Journal 84, 1328–1336.

de Cougny, H.L., Shephard, M.S., 1999. Parallel refinement and coarsening of tetrahedral meshes. International Journal for Numerical Methods in Engineering 46, 1101–1125.

Doblare, M., Cueto, E., Calvo, B., Martinez, M.A., Garcia, J.M., Cegonino, J., 2005. On the employ of meshless methods in biomechanics. Computer Methods in Applied Mechanics and Engineering 194, 801–821.

Dong, C., Skalak, R., 1992. Leukocyte deformability: finite element modeling of large viscoelastic deformation. Journal of Theoretical Biology 158, 173–193.

Drury, J.L., Dembo, M., 2001. Aspiration of human neutrophils: effects of shear thinning and cortical dissipation. Biophysics Journal 81, 3166–3177.

Feng, H., Van Wijngaart, R.D., Biswas, R., 2005. Unstructured adaptive meshes: bad for your memory? Applied Numerical Mathematics 52, 153–173.

Fournier, N., Doillon, C.J., 1992. In vitro angiogenesis in fibrin matrices containing fibronectin or hyaluronic acid. Cell Biology International Report 16, 1251–1263.

Gropp, W., Lusk, E., Doss, N., Skjellum, A., 1996. A high-performance, portable implementation of the MPI message passing interface standard. Parallel Computing 22, 789–828.

Guilak, F., Jones, W.R., Ting-Beall, H.P., Lee, G.M., 1999. The deformation behavior and mechanical properties of chondrocytes in articular cartilage. Osteoarthritis Cartilage 7, 59–70.

Guilkey, J.E., Weiss, J.A., 2003. Implicit time integration for the Material Point Method: Quantitative and algorithmic comparisons with the Finite Element Method. International Journal for Numerical Methods in Engineering 57, 1323–1338.

Harlow, F.H., 1964. The particle-in-cell computing method for fluid dynamics. In: Alder, S.F.B., Rotenberg, M. (Eds.), Methods for Computational Physics, pp. 319–343.

Hoying, J.B., Boswell, C.A., Williams, S.K., 1996. Angiogenic potential of microvessel fragments established in three-dimensional collagen gels. In Vitro Cellular and Developmental Biology 32, 402–419.

Karcher, H., Lammerding, J., Huang, H., Lee, R.T., Kamm, R.D., Kaazempur-Mofrad, M.R., 2003. A three-dimensional viscoelastic model for cell deformation with experimental verification. Biophysics Journal 85, 3336–3349.

Korff, T., Augustin, H.G., 1999. Tensional forces in fibrillar extracellular matrices control directional capillary sprouting. Journal of Cell Science 112 (Pt 19), 3249–3258.

Krishnan, L., Song, H., Hoying, J.B., Das, R., Weiss, J.A., 2003a. Angiogenesis alters the material properties of the extracellular matrix. Proceedings of the 49th Annual Orthopaedic Research Society Meeting 28, 278.

Krishnan, L., Song, H., Hoying, J.B., Weiss, J.A., 2003b. Effects of angiogenesis on the material properties of the extracellular matrix: Correlation with gene expression. Proceedings of the ASME Summer Bioengineering Conference, 949–950.

Krishnan, L., Weiss, J.A., Wessman, M.D., Hoying, J.B., 2004. Viscoelastic characterization of collagen gels for culture of tissues and cells. Tissue Engineering 10, 241–252.

Lei, X., Lawrence, M.B., Dong, C., 1999. Influence of cell deformation on leukocyte rolling adhesion in shear flow. Journal of Biomechanical Engineering 121, 636–643.

Li, S., Liu, W.K., 2002. Meshfree and particle methods and their applications. Applied Mechanics Review 55, 1–34.

Parker, S., 2002. A component-based architecture for parallel multiphysics PDE simulation. In: Sloot, P.M.A., et al. (Eds.), International Conference on Computational Science (ICCS2002) Workshop on PDE Software. pp. 719–734.

Prajapati, R.T., Chavally Mis, B., Herbage, D., Eastwood, M., Brown, R.A., 2000. Mechanical loading regulates protease production by fibroblasts in three-dimensional collagen substrates. Wound Repair and Regeneration 8, 226–237.

Seliktar, D., Black, R.A., Vito, R.P., Nerem, R.M., 2000. Dynamic mechanical conditioning of collagen-gel blood vessel constructs induces remodeling in vitro. Annals of Biomedical Engineering 28, 351–362.

Shao, J.Y., 2002. Finite element analysis of imposing femtonewton forces with micropipette aspiration. Annals of Biomedical Engineering 30, 546–554.

Shepherd, B.R., Chen, H.Y., Smith, C.M., Gruionu, G., Williams, S.K., Hoying, J.B., 2004. Rapid perfusion and network remodeling in a microvascular construct after implantation. Arteriosclerosis Thrombosis and Vascular Biology 24, 898–904.

Simo, J.C., Hughes, T.J.R., 1998. Computational Inelasticity. New York.

Spector, A.A., Ameen, M., Charalambides, P.G., Popel, A.S., 2002. Nanostructure, effective properties, and deformation pattern of the cochlear outer hair cell cytoskeleton. Journal of Biomechanical Engineering 124, 180–187.

Sulsky, D., Chen, Z., Schreyer, H.L., 1994. A particle method for history dependent materials. Computer Methods in Applied Mechanics and Engineering 118, 179–196.

Sulsky, D., Zhou, S., Schreyer, H.L., 1995. Application of a particle-in-cell method to solid mechanics. Computer Physics Communications 87, 236–252.

Volokh, K.Y., Vilnay, O., Belsky, M., 2002. Cell cytoskeleton and tensegrity. Biorheology 39, 63–67.

Wakatsuki, T., Kolodney, M.S., Zahalak, G.I., Elson, E.L., 2000. Cell mechanics studied by a reconstituted model tissue. Biophysics Jouranl 79, 2353–2368.

Wissink, A.M., Hysom, D., Hornung, R.D., 2003. Enhancing Scalability of Parallel Structured AMR Calculations. Presented at 2003 International Conference on Supercomputing, June 23–26 2003, San Francisco, CA, United States.

Wu, J.Z., Herzog, W., 2000. Finite element simulation of location- and time-dependent mechanical behavior of chondrocytes in unconfined compression tests. Annals Biomedical Engineering 28, 318–330.

Zhou, S., 1998. The numerical prediction of material failure based on the material point method. Ph.D. thesis. University of New Mexico, Albuquerque.

Zhu, W.-H., Guo, X., Villaschi, S., Nicosia, R.F., 2000. Regulation of vascular growth and regression by matrix metalloproteinases in the rat aorta model of angiogenesis. Laboratory Investigation 80, 545–555.